ACS NANO

www.acsnano.org

Article

Nanoscale Manipulation of the Local Kondo Effect in an Artificial Heavy-Fermion System

Qiuchen Yu,[#] Peng Fan,[*,#] Ziyuan Liu,[#] Hui Guo,[#] Jiayi Wang, Zhongyi Cao, Hui Chen, Kai Yang,[*] Lizhi Zhang,[*] and Hong-Jun Gao[*]

Cite This: *ACS Nano* 2026, 20, 9205−9213

Read Online

ACCESS | Metrics & More | Article Recommendations | Supporting Information

ABSTRACT: Two-dimensional (2D) van der Waals heterostructures based on *d*-electron materials offer a platform for realizing heavy-Fermion systems with Kondo lattices. However, the nondestructive and reversible manipulation of spins at the nanoscale in 2D heavy-Fermion materials—essential for their application in spintronic devices—remains elusive. In this paper, we successfully manipulate and characterize both spin (Kondo effects) and electronic (charge density wave) degrees of freedom in the 2D heavy-Fermion system of 1T/1H-$TaSe_2$ heterostructure using scanning tunneling microscopy/spectroscopy (STM/STS). By applying voltage pulses, we precisely control the chirality and arrangement of the charge density wave coupled with local spins in 1T-$TaSe_2$. This process also leads to the generation and annihilation of two distinct types of domain walls (DWs). Combining STS and first-principles calculations, we reveal that the local spins are quenched in the type-II DW, which forms between two domains exhibiting a phase shift yet possessing identical chirality. This results in the disappearance of the Kondo resonance. The Mott phase also quenches within type-II DWs. Our results demonstrate a nondestructive and reversible approach to manipulate and understand the local spins of the Kondo lattice in artificial 2D heavy-Fermion systems with nanoscale precision.

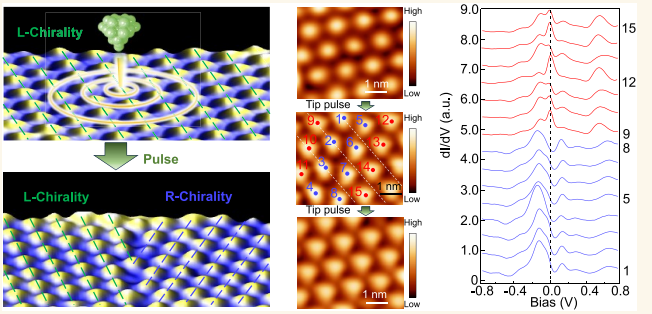

KEYWORDS: *Kondo lattice, spin, domain wall, scanning tunneling microscopy (STM), tantalum diselenide*

Exchange coupling between itinerant electrons and local magnetic moments, such as those from the d- or f-electron, gives rise to the heavy-Fermion phenomenon in Kondo lattice systems. Well-known heavy-Fermion materials include bulk f-electron systems involving actinide- and lanthanide-based compounds,[1−4] bulk d-electron compounds such as LiV_2O_4,[5] and Fe_3GeTe_2,[6] as well as two-dimensional (2D) magic-angle twisted Moiré superlattices.[7,8] In these heavy-Fermion systems, the interplay between Kondo screening and Ruderman−Kittel−Kasuya−Yosida (RKKY) spin interactions can be tuned by pressure,[9,10] chemical doping,[11] magnetic field,[12] and gate voltage.[7] Tuning the interplay between the Kondo screening and RKKY interactions can produce a variety of many-body quantum phenomena, ranging from magnetic ordered ground state,[13,14] heavy Fermi liquid,[15] and unconventional superconductivity[16−18] to quantum criticality.[9,19,20] However, to the best of our knowledge, previous tuning methods have been global in nature. Nondestructive and reversible tuning of local spins and electronic properties at the nanoscale is essential for better understanding and application of heavy-Fermion materials, but it remains challenging. 2D heavy-Fermion materials offer distinct benefits for creating gateable devices and heterostructures to manipulate the emergent quantum phenomenon. Thus, further studies based on 2D heavy-Fermion systems are essential.

2D artificial van der Waals heterostructures constructed by a *d*-electron material (1T-TaS_2, 1T-$TaSe_2$, or 1T-$NbSe_2$) and an electron bath have emerged as new and tunable heavy-Fermion platforms featuring Kondo lattices.[21−29] In these systems, the 1T monolayer is a correlated Mott insulator with star-of-David charge density waves (CDW).[22,30−33] Each star-of-David pattern has one unpaired electron, providing a localized spin and forming a triangular spin−lattice.[21,24,34,35] When the 1T monolayer couples with a metal, the hybridization between the local spins and itinerant electrons induces periodic Kondo resonance, giving rise to the formation of a Kondo lattice. Previous studies have primarily focused on the electrical manipulation of CDW electronic states in 1T monolayers,[35−38] while the evolution of local spin states in the star-of-David patterns before and after the CDW manipulation has not yet

Received: October 28, 2025
Revised: February 22, 2026
Accepted: February 24, 2026
Published: March 9, 2026

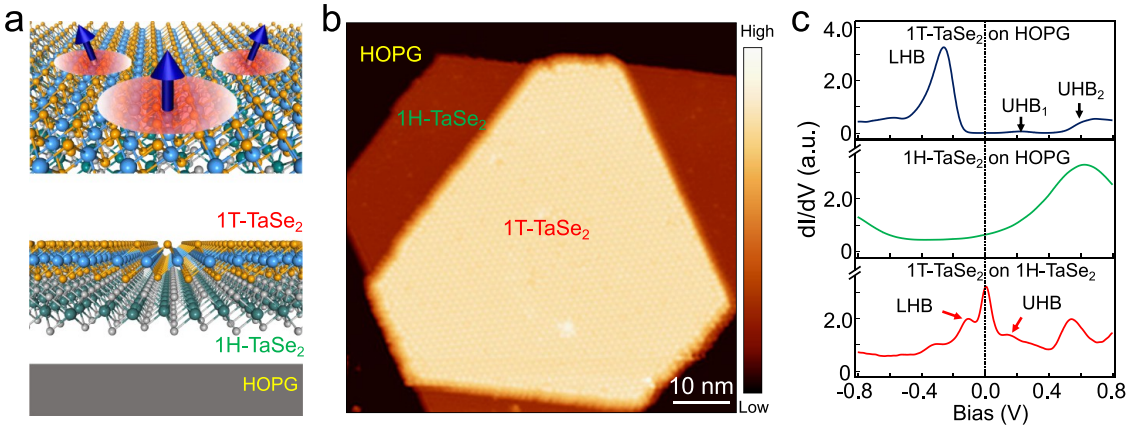

Figure 1. Topography and electronic properties of the 1T/1H-$TaSe_2$ heterostructure. (a) Schematic of the 1T/1H-$TaSe_2$ heterostructure grown on HOPG. The blue arrows indicate the local spins in 1T-$TaSe_2$. (b) STM image (I_t = 100 pA, V_s = −1 V) of a 1T/1H-$TaSe_2$ vertical heterostructure on the HOPG substrate detected at 5.7 K. (c) STS (I_t = 100 pA, V_s = −1 V) detected on the 1T-$TaSe_2$ single layer (blue curve), 1H-$TaSe_2$ single layer (green curve) and 1T/1H-$TaSe_2$ heterostructure (red curve) at 5.7 K, respectively. Lower Hubbard band (LHB) and upper Hubbard band (UHB) are labeled.

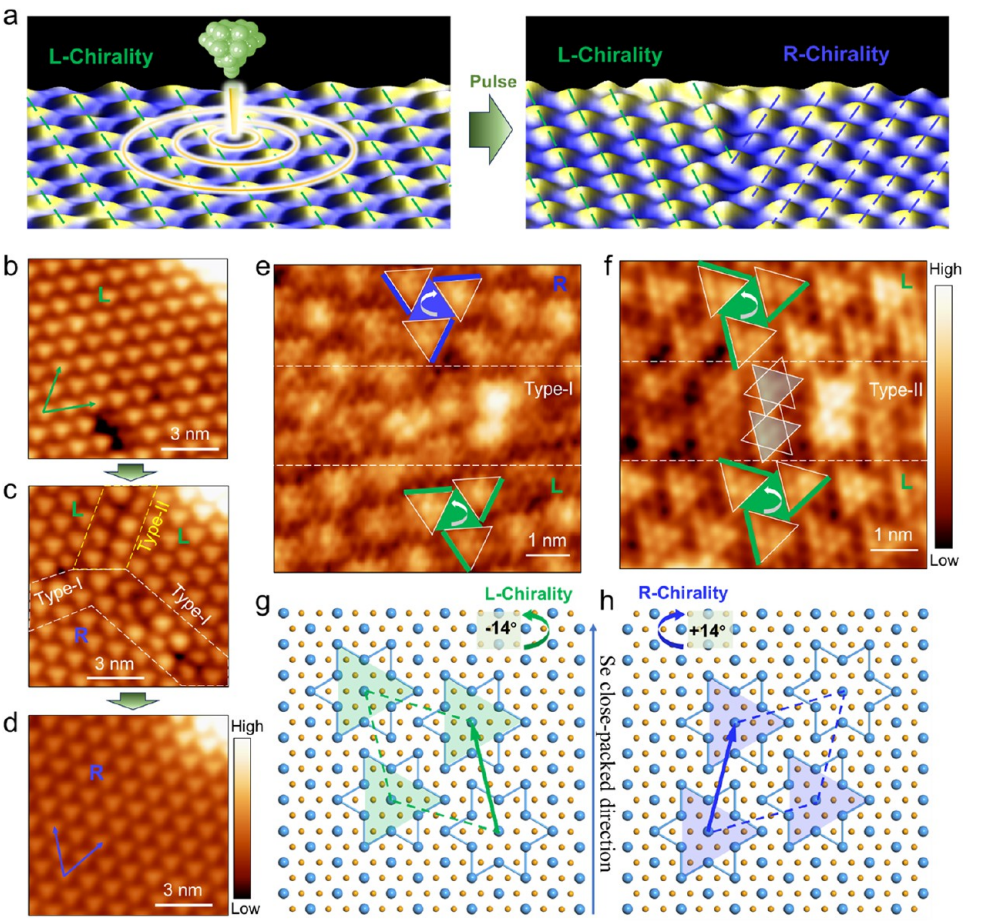

Figure 2. Nanoscale manipulation of the CDW in the 1T/1H-$TaSe_2$ heterostructure. (a) Schematic of the manipulating process by voltage pulses. The orientation (highlighted by dashed green and blue lines) and chirality of the CDW are changed. (b–d) Sequence of STM images (I_t = 100 pA, V_s = −1 V) detected at 5.7 K shows the manipulation of the CDW. Two types of CDW domain walls (DWs) (highlighted by dashed white (type-I) and yellow (type-II) lines) are created. The green and blue arrows trace the CDW lattice directions. (e, f) STM images of type-I (e) (I_t = 20 pA, V_s = 5 mV) and type-II (f) (I_t = 20 pA, V_s = −20 mV) DWs detected at 5.7 K. The star-of-David patterns are highlighted by triangles. The green (blue) highlights the left (right) chirality, respectively. (g, h) Atomic models of the left- (g) and right-chiral (h) CDW phases, respectively. The green (g) and blue (h) arrows indicate the CDW close-packed directions, which are rotated by ± 14° with respect to the top Se atom close-packed direction.

been explored in the artificial 2D heavy-Fermion heterostructures.

In this work, we successfully achieve nondestructive and reversible tuning and characterization of the local Kondo

https://doi.org/10.1021/acsnano.5c18660
ACS Nano 2026, 20, 9205−9213

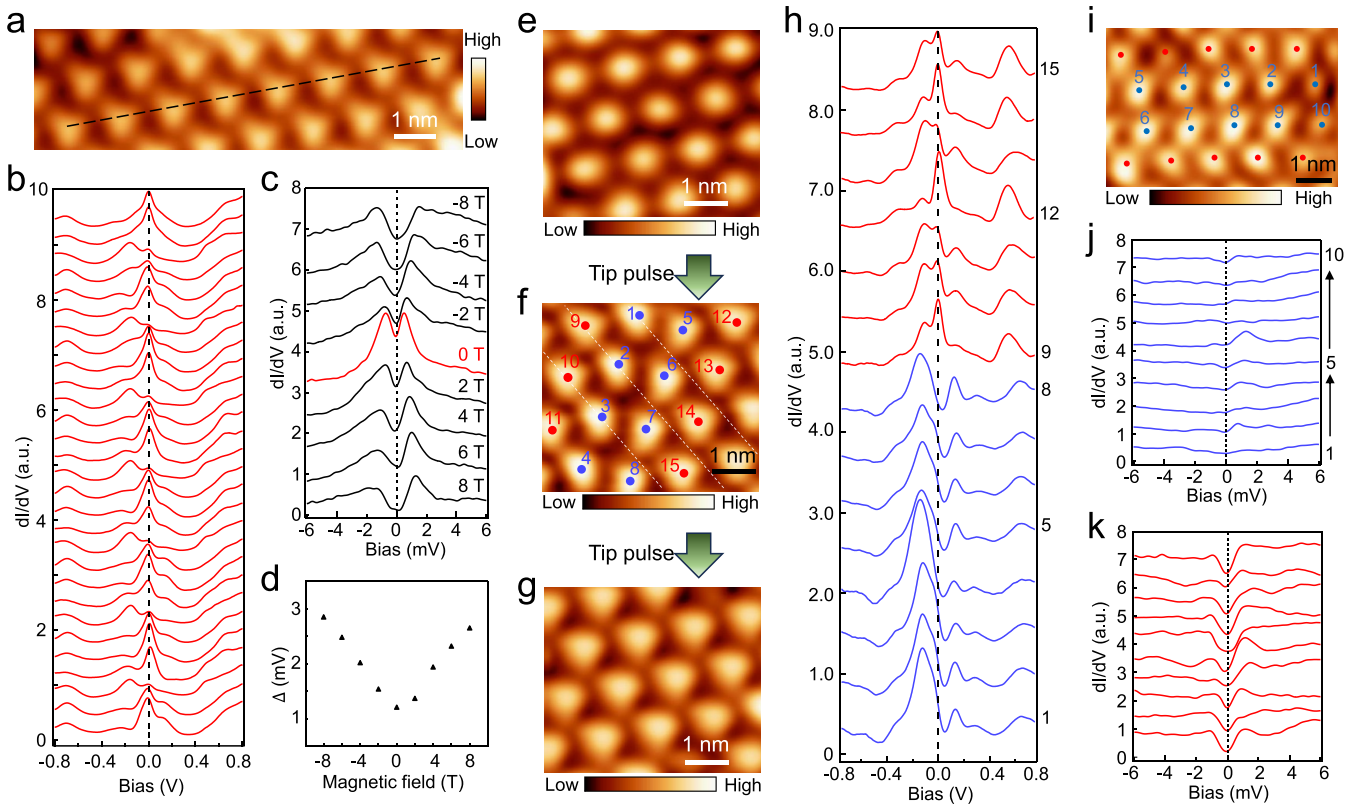

Figure 3. Electronic properties of Kondo lattices before and after the manipulation. (a) STM image (I_t = 100 pA, V_s = −1 V) of the 1T/1H-$TaSe_2$ heterostructure detected at 5.7 K. (b) Series of STS (I_t = 100 pA, V_s = −1 V) detected at 5.7 K along the dashed black line in panel (a). (c) Evolution of dI/dV spectra (I_t = 50 pA, V_s = −10 mV) with an out-of-plane magnetic field, measured at the center of the star-of-David pattern at 0.4 K. (d) Plot of peak separation Δ as a function of the magnetic field. (e−g) Sequence of STM images (I_t = 100 pA, V_s = −1 V) detected at 5.7 K shows the nondestructive generation and annihilation of the type-II DW. The dashed white lines in panel (f) trace the CDW lattice. (h) Series of STS (15 spectra) (I_t = 100 pA, V_s = −1 V) detected at 5.7 K at the center of the star-of-David patterns labeled in panel (f). The red curves are detected in normal star-of-David patterns located off the DW. The blue curves are detected in star-of-David patterns located on the DW. (i) STM image (I_t = 100 pA, V_s = −1 V) of a type-II DW in the 1T/1H-$TaSe_2$ heterostructure detected at 0.4 K. (j) Waterfall-like plot of 10 spectra (I_t = 50 pA, V_s = −10 mV) detected at 0.4 K at the center of star-of-David patterns within the type-II DW labeled in panel (i). (k) Waterfall-like plot of spectra (I_t = 50 pA, V_s = −10 mV) detected at 0.4 K at the center of star-of-David patterns near the type-II DW labeled in panel (i).

effects at the nanoscale in the 1T/1H-$TaSe_2$ heterostructure by employing low-temperature scanning tunneling microscope/spectroscopy (STM/STS). The chirality and arrangement of the CDW are nondestructively manipulated and two types of domain walls (DWs) of CDW are created and annihilated by voltage pulses. Type-I DWs form between two CDW domains with different chiralities, whereas type-II DWs form between two CDW domains with the same chirality but with a phase shift. Owing to the coexisting localized spins with the star-of-David patterns, the spin−lattice changes along with the manipulation of the CDW. We find that Kondo resonance is absent in the STS obtained from type-II DWs, where the spin quenches within the DWs as confirmed by the first-principles calculations. The Mott phase is also annihilated within type-II DWs. Furthermore, we also demonstrate that the generation and annihilation of DWs are reversible, allowing for the controllable switching of the Kondo resonance.

RESULTS

The 1T-$TaSe_2$ undergoes an incommensurate CDW phase transition at 600 K and then transits to the $\sqrt{13} \times \sqrt{13}$ commensurate CDW phase at 473 K.[39] Previous works indicated that the electrons of the topmost layers localize in a Mott phase below 250 K for bulk and below 450 K for the single layer.[40,41] A Kondo peak has been observed in 1T/1H-$TaSe_2$ heterobilayers with Kondo transition temperature T_K at 57 K.[21] Our experiments are carried out on high-quality 1T/1H-$TaSe_2$ heterostructures grown on highly oriented pyrolytic graphite (HOPG) by means of molecular beam epitaxy (Figure 1a,b). The measured STS for 1T- and 1H-$TaSe_2$ monolayers, as well as for the 1T/1H-$TaSe_2$ heterostructure are displayed in Figure 1c. The 1T-$TaSe_2$ monolayer exhibits characteristics of a Mott insulator, featuring lower Hubbard bands (LHB) at $V \approx -0.25$ V and upper Hubbard bands (UHB) at $V \approx 0.23$ V (UHB_1) and $V \approx 0.67$ V (UHB_2). The 1H-$TaSe_2$ monolayer is a metal with a finite local density of states (DOSs) at the Fermi level, serving as an electron bath in the heterostructure. The STS detected on the 1T/1H-$TaSe_2$ heterostructure shows a strong peak at zero energy, indicating the presence of the Kondo effect. The two weaker peaks (highlighted by red arrows in Figure 1c) below and above the Fermi level correspond to the LHB at $V \approx -0.11$ V and UHB at $V \approx 0.15$ V, which are consistent with a previous work.[23]

Next, we show nanoscale manipulation of the CDW with voltage pulses applied in the STM junction, as schematically shown in Figure 2a. We first positioned the STM tip above the destination site at a set point tunneling current of 100 pA (DC bias is +1 V). Then, the tip−sample distance is reduced by 0.4 nm with the feedback loop open. This step is aimed at

https://doi.org/10.1021/acsnano.5c18660
ACS Nano 2026, 20, 9205−9213

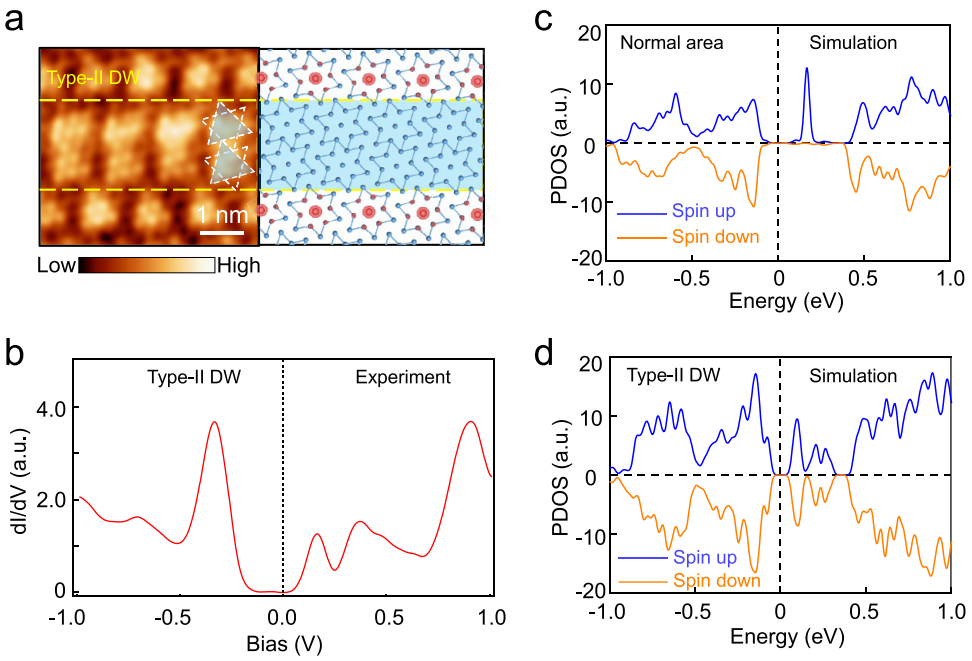

Figure 4. Spin properties of the type-II domain wall within the 1T-$TaSe_2$ single layer on a HOPG. (a) STM image (I_t = 20 pA, V_s = 5 mV) of the type-II DW detected at 5.7 K and its schematic structural configuration of the 1T-$TaSe_2$ single layer on HOPG. The red solid circles indicate spin charge distributions of star-of-David patterns near the type-II DW within the energy range of 0.13−0.22 eV at an isosurface level of 0.003 e/Å^3. (b) STS (I_t = 100 pA, V_s = −1 V) detected at 5.7 K at the center of the star-of-David pattern in the type-II DW on the 1T-$TaSe_2$ single layer on HOPG. (c) Calculated spin-resolved PDOSs at the 13 Ta atoms within the normal star-of-David pattern near the type-II DW. (d) Calculated spin-resolved PDOS at 24 Ta atoms in the type-II DW.

increasing the tunneling current (10 μA), which can effectively reduce the working pulse voltage. Finally, a voltage pulse of 1.8 V is applied for 500 ms, with a maximum current of approximately 80 μA. After applying the voltage pulse, multiple CDW domains are generated in Figure 2c. After an additional voltage pulse of the same parameter near the DW, a perfect CDW lattice is restored (Figure 2d) but with an orientation entirely distinct from that in Figure 2b, suggesting the absence of structural defects induced by the voltage pulses. Note that the CDW depression in Figure 2b recovered after manipulation, possibly due to charge redistribution. The Kondo lattices should also undergo variations corresponding to the CDW period due to the binding between local spins and star-of-David patterns, which is confirmed in Figure 3. We further demonstrate the precise control of type-II DWs in Figure S1. By applying pulses multiple times, the DW generated and moved from left to right with the step adjusted to a single period of the CDW. This shows a potential way to precisely control the DW. The reversible generation and annihilation of type-I DW is also shown in Figure S2. The sample was maintained at 5.7 K for several days, and no spontaneous annihilation of the DWs was observed. The absence of any change over this period indicates that the DWs are stable at this temperature.

A more detailed study of the manipulation process is elaborated in the Methods section and Figures S3 and S4. In our manipulation process, both a high electric field and a large current are required to move the DW, and we conclude that the sudden local heating caused by electrons/holes may disrupt the CDW lattices around the pulsed region, which could then rearrange once the area cools down. Both negative and positive voltages can trigger the transition of the DWs, and higher voltages can also increase the success rate of the manipulation (Figure S4).

In addition, we also achieved the manipulation of the chirality of CDW in real space, as shown in Figure 2e,2f. Chiral CDW has also been observed in 1T-TaS_2[42,43] and 1T-$NbSe_2$.[37] In the atomically resolved STM image of the type-I DW (Figure 2e), we highlighted the star-of-David patterns with triangles. The star-of-David patterns on the upper side of the type-I DW are arranged clockwise, termed as right chirality, whereas on the lower side, they are arranged counterclockwise, termed as left chirality. In contrast, the star-of-David patterns on the two sides of the type-II DW have the same chirality (Figure 2f). Furthermore, we illustrate the chirality by the atomic model in Figure 2g,h. The directions of the chiral CDW are rotated by −14° (left chirality) and +14° (right chirality) with respect to the close-packed direction of top-layer Se atoms. Depending on the chirality of the CDW, the resulting DWs can be categorized into two types. Type-I arises between two domains with different chiralities, while type-II forms between two domains exhibiting a phase shift yet possessing identical chirality.

As seen from the atomically resolved STM image in Figure 2e, the CDW patterns on the type-I DW have different configurations at different areas. As a result, the dI/dV spectra measured on the type-I DW on the heterostructure (Figure S5) and the 1T-$TaSe_2$ single layer (Figure S6) show strong spatial dependence. Due to the strong inhomogeneity, further understanding of the spectroscopic features in the type-I DW is challenging. In this work, we mainly focused on the type-II DW, where the CDWs have good periodicity.

To investigate the evolution of the Mott states and the behavior of the Kondo lattice before and after the reversible manipulation of the type-II DW, we carried out the STS

https://doi.org/10.1021/acsnano.5c18660
ACS Nano 2026, 20, 9205−9213

measurement in situ (Figure 3). We first detected the STS along the CDW basis vector in the 1T/1H-$TaSe_2$ heterostructure with a perfect CDW period (Figure 3a). Each STS exhibits a pronounced DOS peak at the Fermi level (Figure 3b), consistent with the Kondo resonance peak. The intensities of the zero-bias peaks (ZBPs) follow the CDW periodicity and reach the maximum at the center of the star-of-David patterns, which have the same distributions with the local spin in the 1T-$TaSe_2$. We also examined ZBP at a lower temperature of 0.4 K (Figure 3c). With improved energy resolution, we revealed the existence of two symmetric peaks near the Fermi level at 0 T (red curve in Figure 3c). The observation of a split Kondo peak suggests that the temperature is lower than the critical temperature T_C of the lattice coherence effects.[23] The split Kondo peak at zero magnetic field suggests a ground state with magnetic order in this coherent Kondo lattice,[23] consistent with the heavy-Fermion system scenario. We detected a broadened ZBP at 5.7 K instead of two splitting peaks due to the reduced energy resolution considering the thermal smearing and additional electric noises of the instrument. To provide more evidence of the Kondo origin of these peaks, we applied an out-of-plane magnetic field and found that the energy separation of the two peaks increased in the dI/dV spectra (Figure 3c,d). The observed Zeeman splitting provides evidence to the existence of the ground state with magnetic order in the Kondo lattice.[23]

We utilize voltage pulses to generate the type-II DW within a single domain and then reversibly remove it (Figure 3e−g). These results demonstrate a reversible switching of the Kondo resonance in the Kondo lattice. After a voltage pulse, the CDW lattice splits into two domains exhibiting a phase shift of half a CDW period between each other, leading to the formation of a type-II DW (Figure 3f). Subsequently, we applied another voltage pulse, causing the DW to vanish and the periodic CDW patterns to be restored (Figure 3g). To investigate the evolution of the Kondo lattice behavior, we detect STS at the center of the star-of-David patterns located both on and off the DW (Figure 3h). Remarkably, the Kondo peaks still exist on star-of-David patterns located off the DW (red curves in Figure 3h), but the zero-bias peak disappears and broad dips emerge near the Fermi level on star-of-David patterns located on the DW (blue curves in Figures 3h and S7). We also performed high-energy-resolution STS measurements at 0.4 K within and near the type-II DW in the 1T/1H-$TaSe_2$ heterostructure (Figure 3i−k). The LDOS near the Fermi energy within the type-II DW is almost flat, while the splitting Kondo peaks still exist within the star-of-David near the DW. Statistically, the absence of the Kondo resonance in type-II DWs has been observed across more than ten islands and six batches of samples.

The hybridization between the 1T-$TaSe_2$ and 1H-$TaSe_2$ single layers could introduce vibrations in the LDOS (blue curves in Figure 3h). In addition, the strongly correlated quantum states in the heterostructure predominantly rely on a 1T-$TaSe_2$ single layer. Therefore, to investigate the properties of the type-II DWs and the mechanism of the disappearance of the Kondo resonance in type-II DWs, we further studied single-layer 1T-$TaSe_2$ on HOPG (Figures 4a,b, S8, and S9). Figure 4a shows the STM image after applying voltage pulses and the corresponding schematic structural configuration. It is apparent that the type-II DW forms, owing to the phase discrepancy of the CDW between the two domains. In addition, each pair of star-of-David patterns shares two Ta atoms and comprises an even number (12 + 12) of Ta atoms, leading to an even number of electrons.[35] Distinctly different from the DW with metal phases studied on the bulk 1T-TaS_2,[35,36] here we observe that there is still a reduced gap in the spectra detected in the type-II DW (Figures 4b and S8). Additionally, we measure conductance maps at different energies on the type-II DW (Figure S9). The intensities of DOSs in the type-II DW at positive energies are relatively stronger than those in the normal area. In contrast, the DOS intensities at negative energies show no clear difference between the DW and normal areas.

Here, we discuss the origination of the gap within the type-II DW on the 1T-$TaSe_2$ single layer. The even number of Ta atoms in the star-of-David patterns is more consistent with a band-insulating state. The disappearance of the Kondo resonance also indicates the annihilation of the Mott phase. It has been pointed out that disorder can reduce the correlation energy.[44,45] This may disrupt the Mott phase. We also carried out the electronic state distributions within the type-II DW (see the constructed DW supercell in Figure S10) without the inclusion of the Hubbard U parameter (Figure S11) and found that there is still a gap in the PDOS. This result also supports the existence of a band-insulating state.

Finally, we focus on the mechanism behind the disappearance of the Kondo resonance in the type-II DW. We can rule out the possibility that the differences in the vertical stacking configurations between the 1T and 1H layers lead to the quenching of the ZBPs.[46−48] The atomic-resolved STM images in Figures 2f and 4a reveal that the type-II DW consists of two rows of CDW patterns and can be divided into upper row and lower row. The upper (lower) row of the DW has the same CDW lattice arrangement as the upper (lower) domain, indicating the same vertical stacking configuration. It is also possible that the voltage pulses modify the 1H-$TaSe_2$ layer underneath the 1T-$TaSe_2$ layer, resulting in the suppression of the Kondo resonance. To check this possibility, we also applied the manipulation process on the 1H-$TaSe_2$ layer on HOPG using the same parameters as those applied to the 1T/1H-$TaSe_2$ heterostructure. However, we did not find any modification of the CDW patterns. Therefore, we can exclude this possibility.

To elucidate the disappearance of the Kondo resonance peaks on the type-II DW, we investigate the electronic and magnetic properties of the star-of-David patterns by using first-principles calculations. The constructed DW supercell with one normal star-of-David and one type-II DW contains 37 Ta atoms and 74 Se atoms (Figure S10). Due to the Ta atoms giving rise to a Mott insulating transition of 1T-$TaSe_2$,[49] we consider the contribution of Ta atoms in the star-of-David patterns near and within the type-II DW. For the normal star-of-David patterns near the type-II DW, the calculated projected density of states (PDOSs) of 13 Ta atoms exhibit spin polarization (Figure 4c), which is consistent with previous results.[21,50] In contrast to the PDOSs of 13 Ta atoms within normal star-of-David patterns near the type-II DW, the calculated PDOSs of 24 Ta atoms in type-II DW are nearly the same between spin-up and spin-down parts within the considered energy range. The equal weight between spin-up and spin-down parts indicates that there is no major magnetic moment in the type-II DW. As a result, the Kondo resonance peaks vanished in the generated type-II DW in the 1T/1H-$TaSe_2$ heterostructure. The calculated spin-polarized charge density in single-layer 1T-$TaSe_2$ in Figure 4a also clearly shows

https://doi.org/10.1021/acsnano.5c18660
ACS Nano 2026, 20, 9205−9213

that there is no spin-polarized charge density distributed around the Ta atoms of the star-of-David patterns in the type-II DW. In contrast, there is spin-polarized charge density distributed around the Ta atoms of the star-of-David patterns near the type-II DW, and the accumulation of charges exhibits a similar distribution pattern compared with normal star-of-David (DW free) (Figure S12). We also construct the DW supercell/1H-$TaSe_2$ heterostructure with 74 Ta atoms and 148 Se atoms (Figure S13) and get the same results for the type-II DW. As shown in Figure 4a, the star-of-David patterns reconstruct compared to a single domain. Each pair shares two Ta atoms, enhancing the electron hopping between them. This may lead to electron pairing, which explains the quenched magnetic moment in the calculation result. This analysis clarifies the presence of Kondo resonances within the domain but their absence within the DW of the heterostructure. The spin-degenerate PDOS is also consistent with the nonmagnetic band-insulator interpretation.

CONCLUSIONS

In summary, we achieved precise control of both the spin (the local Kondo effects) and electronic (CDW) degrees of freedom in the 1T/1H-$TaSe_2$ heterostructure. The reversible generation and annihilation of the local spins at the nanoscale have never been achieved in Kondo lattice systems. This work provides a nondestructive and reversible strategy to manipulate the local spins of the Kondo lattice and could be applicable for spintronic devices based on 2D heavy-Fermion materials. In addition, by constructing a 1T-$TaSe_2$ single layer on a superconductor or topological materials, our technique can also be employed to manipulate other possible strongly correlated phenomena, such as Majorana zero modes[51] and Yu−Shiba−Rusinov lattices.[52]

METHODS

Sample Preparation

1T/1H-$TaSe_2$ heterostructures were grown on cleaved highly ordered pyrolytic graphite (HOPG) substrates by molecular beam epitaxy (MBE) in an ultrahigh vacuum chamber (UHV, base pressure ~3×10^{-10} mbar). High-purity tantalum (99.9%, Goodfellow Cambridge Ltd.) and selenium (99.999%, Sigma-Aldrich) were evaporated from an e-beam evaporator and a Knudsen cell, respectively. During the growth, the substrates were kept at 530 °C, which was higher than the growth temperature of the pure 1H-$TaSe_2$ phase to obtain the 1T-$TaSe_2$/1H-$TaSe_2$ heterostructure. The growth rate was about 2 h per monolayer and the Se flux was kept approximately an order of magnitude greater than the Ta flux (Se-rich conditions). After the codeposition, the substrates were kept at 250 °C for an hour to remove extra Se atoms.

Scanning Tunneling Microscopy/Spectroscopy

STM/STS data were acquired in a commercial UHV-STM system (CASAcme Technology) and a commercial UHV-STM system equipped with perpendicular magnetic fields up to 11 T (Unisoku, USM1300). The samples are covered with Se layers with a height of about 10 nm and transferred into an STM by using an isolated high-vacuum (1×10^{-9} mbar) chamber with loading and unloading functions. After transfer into the STM chamber, the samples are annealed at 200 °C to remove the Se atoms. The STM experiments on the 1T-$TaSe_2$/1H-$TaSe_2$ heterostructure are carried out at temperature between 0.4 and 5.7 K in an ultrahigh vacuum (~1×10^{-11} mbar) LT-STM system in the constant-current mode with a tungsten tip, which is calibrated on a clean Au(111) surface. STS are acquired by a standard lock-in amplifier at a frequency of 973.1 Hz, under the modulation voltages V_{mod} = 20 mV at 5.7 K and V_{mod} = 0.05 mV at 0.4 K.

Manipulation Process

In our work, a pulse voltage/separation/current of 1.9 V/0.55 nm/1 nA could move the DW, while a pulse voltage/separation/current of 7.4 V/1.3 nm/0.08 nA with reduced current and increased electric field cannot trigger the movement. This result indicates the important role of a large current during the manipulation. In addition, we studied the threshold current by varying the tip−sample separation at a constant pulse voltage (Figure S3) and found that the threshold current value is about 1 nA. Second, we further studied the effect of a pure current injection (up to 40 μA at a pulse voltage less than 0.2 V) through the point contact between the STM tip and sample without the presence of a large electric field. We found that the DW did not move. Therefore, a large electric field is also required. Furthermore, we found that both positive and negative pulse voltages can move the DWs. The temperature measurement point and the sample are separated by a 3-mm-thick metal sample holder. The refrigeration power of our instrument is about 0.3 W. During the manipulation, the highest power of the voltage pulses is 0.2 mW ($2 \text{ V} \times 1 \times 10^{-4}$ A). As a result, we did not see any difference in the sample temperature during the manipulation. However, we can infer that the temperature changes very quickly. Since both a high electric field and a large current are required to move the DW, we conclude that the sudden local heating caused by electrons and holes may disrupt the CDW lattices around the pulsed region, which could then rearrange once the area cools down. In our experiment, the success rate increases with increasing bias voltages of the pulses and reaches 50−75% in the bias range of 1.6−1.9 V (Figure S4). Further increase of the bias voltage would result in the damage of the tip or the sample. In addition, the success rate depends on the condition of the tip and samples as well as the position where the pulse is applied. The probability to generate type-I DW is about 57.5%, while the probability to generate type-II DW is about 42.5%. Once a DW is generated in a clean area, further voltage pulses with the setting parameters in our work typically do not create more DWs in the same area. Instead, further pulses usually alter the type or location of the existing DW or cause annihilation of the DW.

First-Principles Calculations

Density functional theory (DFT) calculations were performed by using the Vienna ab initio simulation package (VASP)[53,54] within the generalized gradient approximation (GGA) of the Perdew−Burke−Ernzerhof (PBE) functional.[55] The plane-wave energy cutoff was set at 500 eV. The DFT + U (U = 2 eV) correction was performed to model the effects of Ta 3d electron correlation.[30] Spin polarization was considered in all of the calculations. DW supercell with one normal star-of-David and one type-II DW contains 37 Ta atoms and 74 Se atoms as shown in Figure S10. DW supercell/1H-$TaSe_2$ heterostructure with 74 Ta atoms and 148 Se atoms is shown in Figure S13a. When performing the structural optimization, Brillouin zones (BZ) of the 1T-$TaSe_2$ unit cell, 1T-$TaSe_2$ star-of-David charge density wave phase, DW supercell, and DW supercell/1H-$TaSe_2$ heterostructure were segmented of $15 \times 15 \times 1$, $3 \times 3 \times 1$, $1 \times 3 \times 1$, and $1 \times 1 \times 1$ γ-centered K-mesh, respectively. A 30 Å vacuum length along the z-direction was set. All the structures were relaxed until energy converged to 10^{-5} eV and the force tolerance on each atom was below 0.01 eV/Å. A γ-centered k-point mesh of $3 \times 6 \times 1$ was adopted to the spin charge distribution and self-consistent and projected density of states calculations of the DW supercell and DW supercell/1H-$TaSe_2$ heterostructure.

ASSOCIATED CONTENT

Supporting Information

The Supporting Information is available free of charge at https://pubs.acs.org/doi/10.1021/acsnano.5c18660.

STM images of the DW manipulation process, test of the manipulation process, dI/dV spectra of both types of

https://doi.org/10.1021/acsnano.5c18660
ACS Nano 2026, 20, 9205−9213

DWs, dI/dV maps of the type-II DW, structure of the calculated supercell, calculated spin-resolved PDOS, and calculated spin-resolved charge distribution (PDF)

DW supercell in 1T and 1H-$TaSe_2$ heterostructure (CIF)

DW supercell in 1T-$TaSe_2$ (CIF)

normal star-of-David unit cell in 1T-$TaSe_2$ (CIF)

AUTHOR INFORMATION

Corresponding Authors

Peng Fan − *Beijing National Center for Condensed Matter Physics and Institute of Physics, Chinese Academy of Sciences, Beijing 100190, P. R. China; School of Physical Sciences, University of Chinese Academy of Sciences, Beijing 100190, P. R. China*; Email: pengf@iphy.ac.cn

Kai Yang − *Beijing National Center for Condensed Matter Physics and Institute of Physics, Chinese Academy of Sciences, Beijing 100190, P. R. China; School of Physical Sciences, University of Chinese Academy of Sciences, Beijing 100190, P. R. China*; Email: kaiyang@iphy.ac.cn

Lizhi Zhang − *National Center for Nanoscience and Technology, Beijing 100190, P. R. China*; Email: zhanglz@nanoctr.cn

Hong-Jun Gao − *Beijing National Center for Condensed Matter Physics and Institute of Physics, Chinese Academy of Sciences, Beijing 100190, P. R. China; School of Physical Sciences, University of Chinese Academy of Sciences, Beijing 100190, P. R. China; Hefei National Laboratory, Hefei, Anhui 230088, P. R. China*; orcid.org/0000-0002-6766-0623; Email: hjgao@iphy.ac.cn

Authors

Qiuchen Yu − *Beijing National Center for Condensed Matter Physics and Institute of Physics, Chinese Academy of Sciences, Beijing 100190, P. R. China; School of Physical Sciences, University of Chinese Academy of Sciences, Beijing 100190, P. R. China*

Ziyuan Liu − *School of Physics and Optoelectronic Engineering, Beijing University of Technology, Beijing 100124, P. R. China; National Center for Nanoscience and Technology, Beijing 100190, P. R. China*

Hui Guo − *Beijing National Center for Condensed Matter Physics and Institute of Physics, Chinese Academy of Sciences, Beijing 100190, P. R. China; School of Physical Sciences, University of Chinese Academy of Sciences, Beijing 100190, P. R. China; Hefei National Laboratory, Hefei, Anhui 230088, P. R. China*

Jiayi Wang − *Beijing National Center for Condensed Matter Physics and Institute of Physics, Chinese Academy of Sciences, Beijing 100190, P. R. China; School of Physical Sciences, University of Chinese Academy of Sciences, Beijing 100190, P. R. China*

Zhongyi Cao − *Beijing National Center for Condensed Matter Physics and Institute of Physics, Chinese Academy of Sciences, Beijing 100190, P. R. China; School of Physical Sciences, University of Chinese Academy of Sciences, Beijing 100190, P. R. China*

Hui Chen − *Beijing National Center for Condensed Matter Physics and Institute of Physics, Chinese Academy of Sciences, Beijing 100190, P. R. China; School of Physical Sciences, University of Chinese Academy of Sciences, Beijing 100190, P. R. China; Hefei National Laboratory, Hefei, Anhui 230088, P. R. China*; orcid.org/0000-0002-3369-8113

Complete contact information is available at: https://pubs.acs.org/10.1021/acsnano.5c18660

Author Contributions

#Q.Y., P.F., Z.L., and H.G. contributed equally to this work. H.-J.G., K.Y., and P.F. designed the experiment. Q.Y., P.F., Z.C., and H.C. carried out the STM measurements. H.G. and J.W. synthesized the samples. Z.L. and L.Z. developed the theoretical model. Q.Y., P.F., K.Y., and H.-J.G. performed the analysis and wrote the manuscript with help from all authors. All authors discussed the results and edited the manuscript.

Notes

The authors declare no competing financial interest.

ACKNOWLEDGMENTS

The work is supported by grants from the CAS Project for Young Scientists in Basic Research (YSBR-003 and YSBR-053), the National Key R&D Program of China (2022YFA1204100 and 2024YFA1207800), the National Natural Science Foundation of China (12474177, 92476202, 12174433, 62488201, 52072401, and 22372047), the Beijing Natural Science Foundation (Z230005), and the Innovation Program of Quantum Science and Technology (2021ZD0302700).

REFERENCES

(1) Stewart, G. R. Heavy-Fermion Systems. *Rev. Mod. Phys.* **1984**, *56*, 755−787.

(2) Wirth, S.; Steglich, F. Exploring Heavy Fermions from Macroscopic to Microscopic Length Scales. *Nat. Rev. Mater.* **2016**, *1*, No. 16051.

(3) Ernst, S.; Kirchner, S.; Krellner, C.; Geibel, C.; Zwicknagl, G.; Steglich, F.; Wirth, S. Emerging Local Kondo Screening and Spatial Coherence in the Heavy-Fermion Metal $YbRh_2Si_2$. *Nature* **2011**, *474*, 362−366.

(4) Aynajian, P.; da Silva Neto, E. H.; Gyenis, A.; Baumbach, R. E.; Thompson, J. D.; Fisk, Z.; Bauer, E. D.; Yazdani, A. Visualizing Heavy Fermions Emerging in a Quantum Critical Kondo Lattice. *Nature* **2012**, *486*, 201−206.

(5) Singh, D. J.; Blaha, P.; Schwarz, K.; Mazin, I. Electronic Structure and Heavy-Fermion Behavior in LiV_2O_4. *Phys. Rev. B* **1999**, *60*, 16359.

(6) Zhang, Y.; Lu, H.; Zhu, X.; Tan, S.; Feng, W.; Liu, Q.; Zhang, W.; Chen, Q.; Liu, Y.; Luo, X. Emergence of Kondo Lattice Behavior in a Van Der Waals Itinerant Ferromagnet, Fe_3GeTe_2. *Sci. Adv.* **2018**, *4*, No. eaao6791.

(7) Zhao, W.; Shen, B.; Tao, Z.; Han, Z.; Kang, K.; Watanabe, K.; Taniguchi, T.; Mak, K. F.; Shan, J. Gate-Tunable Heavy Fermions in a Moire Kondo Lattice. *Nature* **2023**, *616*, 61−65.

(8) Ramires, A.; Lado, J. L. Emulating Heavy Fermions in Twisted Trilayer Graphene. *Phys. Rev. Lett.* **2021**, *127*, No. 026401.

(9) Park, T.; Ronning, F.; Yuan, H. Q.; Salamon, M. B.; Movshovich, R.; Sarrao, J. L.; Thompson, J. D. Hidden Magnetism and Quantum Criticality in the Heavy Fermion Superconductor $CeRhIn_5$. *Nature* **2006**, *440*, 65−68.

(10) Kimura, N.; Ito, K.; Saitoh, K.; Umeda, Y.; Aoki, H.; Terashima, T. Pressure-Induced Superconductivity in Noncentrosymmetric Heavy-Fermion $CeRhSi_3$. *Phys. Rev. Lett.* **2005**, *95*, No. 247004.

(11) Steppke, A.; Küchler, R.; Lausberg, S.; Lengyel, E.; Steinke, L.; Borth, R.; Lühmann, T.; Krellner, C.; Nicklas, M.; Geibel, C.; et al. Ferromagnetic Quantum Critical Point in the Heavy-Fermion Metal $YbNi_4(P_{1-x}As_x)_2$. *Science* **2013**, *339*, 933−936.

(12) Paschen, S.; Lühmann, T.; Wirth, S.; Gegenwart, P.; Trovarelli, O.; Geibel, C.; Steglich, F.; Coleman, P.; Si, Q. Hall-Effect Evolution across a Heavy-Fermion Quantum Critical Point. *Nature* **2004**, *432*, 881−885.
(13) Schröder, A.; Aeppli, G.; Coldea, R.; Adams, M.; Stockert, O.; Löhneysen, H.; Bucher, E.; Ramazashvili, R.; Coleman, P. Onset of Antiferromagnetism in Heavy-Fermion Metals. *Nature* **2000**, *407*, 351−355.
(14) Löhneysen, H. v.; Rosch, A.; Vojta, M.; Wölfle, P. Fermi-Liquid Instabilities at Magnetic Quantum Phase Transitions. *Rev. Mod. Phys.* **2007**, *79*, 1015−1075.
(15) Auerbach, A.; Levin, K. Kondo Bosons and the Kondo Lattice: Microscopic Basis for the Heavy Fermi Liquid. *Phys. Rev. Lett.* **1986**, *57*, 877−880.
(16) Pfleiderer, C. Superconducting Phases of f-Electron Compounds. *Rev. Mod. Phys.* **2009**, *81*, 1551−1624.
(17) Mathur, N. D.; Grosche, F.; Julian, S.; Walker, I.; Freye, D.; Haselwimmer, R.; Lonzarich, G. Magnetically Mediated Superconductivity in Heavy Fermion Compounds. *Nature* **1998**, *394*, 39−43.
(18) Jiao, L.; Howard, S.; Ran, S.; Wang, Z.; Rodriguez, J. O.; Sigrist, M.; Wang, Z.; Butch, N. P.; Madhavan, V. Chiral Superconductivity in Heavy-Fermion Metal UTe_2. *Nature* **2020**, *579*, 523−527.
(19) Gegenwart, P.; Si, Q.; Steglich, F. Quantum Criticality in Heavy-Fermion Metals. *Nat. Phys.* **2008**, *4*, 186−197.
(20) Si, Q.; Steglich, F. Heavy Fermions and Quantum Phase Transitions. *Science* **2010**, *329*, 1161−1166.
(21) Ruan, W.; Chen, Y.; Tang, S.; Hwang, J.; Tsai, H.-Z.; Lee, R. L.; Wu, M.; Ryu, H.; Kahn, S.; Liou, F.; Jia, C.; Aikawa, A.; Hwang, C.; Wang, F.; Choi, Y.; Louie, S. G.; Lee, P. A.; Shen, Z.-X.; Mo, S.-K.; Crommie, M. F. Evidence for Quantum Spin Liquid Behaviour in Single-Layer 1T-$TaSe_2$ from Scanning Tunnelling Microscopy. *Nat. Phys.* **2021**, *17*, 1154−1161.
(22) Vaňo, V.; Amini, M.; Ganguli, S. C.; Chen, G.; Lado, J. L.; Kezilebieke, S.; Liljeroth, P. Artificial Heavy Fermions in a Van Der Waals Heterostructure. *Nature* **2021**, *599*, 582−586.
(23) Wan, W.; Harsh, R.; Meninno, A.; Dreher, P.; Sajan, S.; Guo, H.; Errea, I.; de Juan, F.; Ugeda, M. M. Evidence for Ground State Coherence in a Two-Dimensional Kondo Lattice. *Nat. Commun.* **2023**, *14*, No. 7005.
(24) Zhang, Q.; He, W. Y.; Zhang, Y.; Chen, Y.; Jia, L.; Hou, Y.; Ji, H.; Yang, H.; Zhang, T.; Liu, L.; Gao, H. J.; Jung, T. A.; Wang, Y. Quantum Spin Liquid Signatures in Monolayer 1T-$NbSe_2$. *Nat. Commun.* **2024**, *15*, No. 2336.
(25) Liu, M.; Leveillee, J.; Lu, S.; Yu, J.; Kim, H.; Tian, C.; Shi, Y.; Lai, K.; Zhang, C.; Giustino, F.; Shih, C. K. Monolayer 1T-$NbSe_2$ As a 2D-Correlated Magnetic Insulator. *Sci. Adv.* **2021**, *7*, No. eabi6339.
(26) Kumar Nayak, A.; Steinbok, A.; Roet, Y.; Koo, J.; Feldman, I.; Almoalem, A.; Kanigel, A.; Yan, B.; Rosch, A.; Avraham, N.; Beidenkopf, H. First-Order Quantum Phase Transition in the Hybrid Metal-Mott Insulator Transition Metal Dichalcogenide 4Hb-TaS_2. *Proc. Natl. Acad. Sci. U.S.A.* **2023**, *120*, No. e2304274120.
(27) Shen, S.; Wen, C.; Kong, P.; Gao, J.; Si, J.; Luo, X.; Lu, W.; Sun, Y.; Chen, G.; Yan, S. Inducing and Tuning Kondo Screening in a Narrow-Electronic-Band System. *Nat. Commun.* **2022**, *13*, No. 2156.
(28) Ayani, C. G.; Pisarra, M.; Ibarburu, I. M.; Garnica, M.; Miranda, R.; Calleja, F.; Martin, F.; Vazquez de Parga, A. L. Probing the Phase Transition to a Coherent 2D Kondo Lattice. *Small* **2024**, *20*, No. 2303275.
(29) Ayani, C. G.; Pisarra, M.; Ibarburu, I. M.; Rebanal, C.; Garnica, M.; Calleja, F.; Martín, F.; Vázquez de Parga, A. L. Electron Delocalization in a 2D Mott Insulator. *Nat. Commun.* **2024**, *15*, No. 10272.
(30) Chen, Y.; Ruan, W.; Wu, M.; Tang, S.; Ryu, H.; Tsai, H.-Z.; Lee, R. L.; Kahn, S.; Liou, F.; Jia, C.; Albertini, O. R.; Xiong, H.; Jia, T.; Liu, Z.; Sobota, J. A.; Liu, A. Y.; Moore, J. E.; Shen, Z.-X.; Louie, S. G.; Mo, S.-K.; Crommie, M. F. Strong Correlations and Orbital Texture in Single-Layer 1T-$TaSe_2$. *Nat. Phys.* **2020**, *16*, 218−224.
(31) Liu, L.; Yang, H.; Huang, Y.; Song, X.; Zhang, Q.; Huang, Z.; Hou, Y.; Chen, Y.; Xu, Z.; Zhang, T.; Wu, X.; Sun, J.; Huang, Y.; Zheng, F.; Li, X.; Yao, Y.; Gao, H. J.; Wang, Y. Direct Identification of Mott Hubbard Band Pattern beyond Charge Density Wave Superlattice in Monolayer 1T-$NbSe_2$. *Nat. Commun.* **2021**, *12*, No. 1978.
(32) Nakata, Y.; Sugawara, K.; Shimizu, R.; Okada, Y.; Han, P.; Hitosugi, T.; Ueno, K.; Sato, T.; Takahashi, T. Monolayer 1T-$NbSe_2$ As a Mott Insulator. *NPG Asia Mater.* **2016**, *8*, No. e321.
(33) Nakata, Y.; Yoshizawa, T.; Sugawara, K.; Umemoto, Y.; Takahashi, T.; Sato, T. Selective Fabrication of Mott-Insulating and Metallic Monolayer $TaSe_2$. *ACS Appl. Nano Mater.* **2018**, *1*, 1456−1460.
(34) Law, K. T.; Lee, P. A. 1T-TaS_2 As a Quantum Spin Liquid. *Proc. Natl. Acad. Sci. U.S.A.* **2017**, *114*, 6996−7000.
(35) Cho, D.; Cheon, S.; Kim, K. S.; Lee, S. H.; Cho, Y. H.; Cheong, S. W.; Yeom, H. W. Nanoscale Manipulation of the Mott Insulating State Coupled to Charge Order in 1T-TaS_2. *Nat. Commun.* **2016**, *7*, No. 10453.
(36) Ma, L.; Ye, C.; Yu, Y.; Lu, X. F.; Niu, X.; Kim, S.; Feng, D.; Tomanek, D.; Son, Y. W.; Chen, X. H.; Zhang, Y. A Metallic Mosaic Phase and the Origin of Mott-Insulating State in 1T-TaS_2. *Nat. Commun.* **2016**, *7*, No. 10956.
(37) Song, X.; Liu, L.; Chen, Y.; Yang, H.; Huang, Z.; Hou, B.; Hou, Y.; Han, X.; Yang, H.; Zhang, Q.; Zhang, T.; Zhou, J.; Huang, Y.; Zhang, Y.; Gao, H. J.; Wang, Y. Atomic-Scale Visualization of Chiral Charge Density Wave Superlattices and Their Reversible Switching. *Nat. Commun.* **2022**, *13*, No. 1843.
(38) Mraz, A.; Diego, M.; Kranjec, A.; Vodeb, J.; Karpov, P.; Gerasimenko, Y.; Ravnik, J.; Vaskivskyi, Y.; Venturini, R.; Kabanov, V.; Lipovsek, B.; Topic, M.; Vaskivskyi, I.; Mihailovic, D. Manipulation of Fractionalized Charge in the Metastable Topologically Entangled State of a Doped Wigner Crystal. *Nat. Commun.* **2023**, *14*, No. 8214.
(39) Di Salvo, F.; Maines, R. G.; Waszczak, J. V.; Schwall, R. E. Preparation and Properties of 1T-$TaSe_2$. *Solid State Commun.* **1974**, *14*, 497−501.
(40) Colonna, S.; Ronci, F.; Cricenti, A.; Perfetti, L.; Berger, H.; Grioni, M. Mott Phase at the Surface of 1T−$TaSe_2$ Observed by Scanning Tunneling Microscopy. *Phys. Rev. Lett.* **2005**, *94*, No. 036405.
(41) Nakata, Y.; Sugawara, K.; Chainani, A.; Oka, H.; Bao, C.; Zhou, S.; Chuang, P.-Y.; Cheng, C.-M.; Kawakami, T.; Saruta, Y.; Fukumura, T.; Zhou, S.; Takahashi, T.; Sato, T. Robust Charge-Density Wave Strengthened by Electron Correlations in Monolayer 1T-$TaSe_2$ and 1T-$NbSe_2$. *Nat. Commun.* **2021**, *12*, No. 5873.
(42) Zhao, Y.; Nie, Z.; Hong, H.; Qiu, X.; Han, S.; Yu, Y.; Liu, M.; Qiu, X.; Liu, K.; Meng, S.; Tong, L.; Zhang, J. Spectroscopic Visualization and Phase Manipulation of Chiral Charge Density Waves in 1T-TaS_2. *Nat. Commun.* **2023**, *14*, No. 2223.
(43) Liu, G.; Qiu, T.; He, K.; Liu, Y.; Lin, D.; Ma, Z.; Huang, Z.; Tang, W.; Xu, J.; Watanabe, K.; Taniguchi, T.; Gao, L.; Wen, J.; Liu, J. M.; Yan, B.; Xi, X. Electrical Switching of Ferro-Rotational Order in Nanometre-Thick 1T-TaS_2 Crystals. *Nat. Nanotechnol.* **2023**, *18*, 854−860.
(44) Heidarian, D.; Trivedi, N. Inhomogeneous Metallic Phase in a Disordered Mott Insulator in Two Dimensions. *Phys. Rev. Lett.* **2004**, *93*, No. 126401.
(45) Lahoud, E.; Meetei, O. N.; Chaska, K. B.; Kanigel, A.; Trivedi, N. Emergence of a Novel Pseudogap Metallic State in a Disordered 2D Mott Insulator. *Phys. Rev. Lett.* **2014**, *112*, No. 206402.
(46) Butler, C. J.; Yoshida, M.; Hanaguri, T.; Iwasa, Y. Mottness versus Unit-Cell Doubling As the Driver of the Insulating State in 1T-TaS_2. *Nat. Commun.* **2020**, *11*, No. 2477.
(47) Park, J. W.; Lee, J.; Yeom, H. W. Stacking and Spin Order in a Van Der Waals Mott Insulator 1T-TaS_2. *Commun. Mater.* **2023**, *4*, No. 99.

https://doi.org/10.1021/acsnano.5c18660
ACS Nano 2026, 20, 9205−9213

(48) Zhang, W.; Wu, Z.; Bu, K.; Fei, Y.; Zheng, Y.; Gao, J.; Luo, X.; Liu, Z.; Sun, Y.-P.; Yin, Y. Reconciling the Bulk Metallic and Surface Insulating State in 1T−$TaSe_2$. *Phys. Rev. B* **2022**, *105*, No. 035110.
(49) Wang, W.; Zhao, B.; Ming, X.; Si, C. Multiple Quantum States Induced in 1T-$TaSe_2$ by Controlling the Stacking Order of Charge Density Waves. *Adv. Funct. Mater.* **2023**, *33*, No. 2214583.
(50) Chen, Y.; He, W.-Y.; Ruan, W.; Hwang, J.; Tang, S.; Lee, R. L.; Wu, M.; Zhu, T.; Zhang, C.; Ryu, H.; Wang, F.; Louie, S. G.; Shen, Z.-X.; Mo, S.-K.; Lee, P. A.; Crommie, M. F. Evidence for a Spinon Kondo Effect in Cobalt Atoms on Single-Layer 1T-$TaSe_2$. *Nat. Phys.* **2022**, *18*, 1335−1340.
(51) Kezilebieke, S.; Huda, M. N.; Vano, V.; Aapro, M.; Ganguli, S. C.; Silveira, O. J.; Glodzik, S.; Foster, A. S.; Ojanen, T.; Liljeroth, P. Topological Superconductivity in a van der Waals Heterostructure. *Nature* **2020**, *588*, 424−428.
(52) Soldini, M. O.; Küster, F.; Wagner, G.; Das, S.; Aldarawsheh, A.; Thomale, R.; Lounis, S.; Parkin, S. S. P.; Sessi, P.; Neupert, T. Two-Dimensional Shiba Lattices As a Possible Platform for Crystalline Topological Superconductivity. *Nat. Phys.* **2023**, *19*, 1848−1854.
(53) Kresse, G.; Hafner, J. Ab Initio Molecular Dynamics for Liquid Metals. *Phys. Rev. B* **1993**, *47*, 558−561.
(54) Kresse, G.; Furthmüller, J. Efficiency of ab-Initio Total Energy Calculations for Metals and Semiconductors Using a Plane-Wave Basis Set. *Comput. Mater. Sci.* **1996**, *6*, 15−50.
(55) Perdew, J. P.; Burke, K.; Ernzerhof, M. Generalized Gradient Approximation Made Simple. *Phys. Rev. Lett.* **1996**, *77*, 3865−3868.

https://doi.org/10.1021/acsnano.5c18660
ACS Nano 2026, 20, 9205−9213